Pseudo Jahn-Teller effect driven displacive ferroelectric transition in GeTe

Changrui Wang,[1] Kaiqi Li,[2] Jian Zhou,[1] and Zhimei Sun[1,*]
[1]School of Materials Science and Engineering, Beihang University, Beijing 100191, China
[2]National Key Laboratory of Spintronics, Hangzhou International Innovation Institute, Beihang University, Hangzhou 311115, China

(Received 30 July 2025; revised 15 March 2026; accepted 25 March 2026; published 25 August 2026)

Unifying local and average structural descriptions in germanium telluride (GeTe) remains a critical challenge, highlighting the long-standing displacive versus order-disorder debate in ferroelectric crystals. In this work, we investigate the real-time atomic dynamics and local structural fluctuations in GeTe by coupling density functional theory (DFT) with large-scale molecular dynamics (MD) simulations driven by neuroevolution potentials (NEPs). Our findings demonstrate a displacive ferroelectric phase transition near the tricritical point. By encompassing the ∼25 Å spatial correlation length, our mesoscale simulations overcome finite-size effects that can induce multistate hopping artifacts. Crucially, the computed longitudinal current correlation function ($C_L(q, \omega)$) lacks a quasielastic peak, effectively ruling out thermally activated discrete jumps. Furthermore, time-resolved Crystal Orbital Hamilton Population (tr-COHP) analysis reveals a femtosecond "seesaw" charge transfer driven by the pseudo-Jahn-Teller effect (PJTE). The apparent local disorder in the cubic phase originates from continuous, large-amplitude anharmonic vibrations on a remarkably flat adiabatic potential energy surface, rather than static multiwell hopping. These results support a "macro-ordered yet micro-disordered" displacive paradigm, providing fundamental insights for rationalizing and tailoring the thermal and optoelectronic properties of IV-VI compounds.

DOI: 10.1103/w7ll-dsct

I. INTRODUCTION

GeTe, a prototypical IV-VI semiconductor, has emerged as a promising material for thermoelectric, ferroelectric, and phase-change memory applications due to its unique electronic structure [1,2]. The nature of its ferroelectric phase transition, however, has long been the subject of intense theoretical debate. Recent computational efforts have laid essential groundwork: Dangić *et al.* [3,4] utilized a Gaussian approximation potential to reproduce the macroscopic structural evolution, while Y. Wang *et al.* [5] detailed the critical role of orbit-lattice coupling via the PJTE. Resolving this debate is crucial for linking atomic lattice dynamics to macroscopic functional performance.

Pristine GeTe undergoes a reversible ferroelectric phase transformation at a Curie temperature (T_c) of around 650 ± 50 K [6–8]. As shown in Fig. 1(a), cubic GeTe crystallizes in a rocksalt structure (space group $Fm\bar{3}m$) with a lattice parameter $a = 6$ Å. In its primitive cell, the central Ge atom coordinates with six equivalent Te neighbors through 3 Å bonds. In contrast, rhombohedral GeTe can be viewed as a Peierls distortion of the cubic phase along its diagonal axis, driven by weak p-orbital interactions (space group $R3m$; $a = 4.19$ Å, $c = 11.04$ Å). Here, the off-centered Ge atom forms three short (2.81 Å) and three long (3.30 Å) bonds with Te atoms [Fig. 1(b)]. This distortion reduces the interaxial angle from 60° to 56.81° via lattice shearing, inducing spontaneous polarization in the Ge/Te sublattices [9]. The phase transition coincides with approximately 1% negative thermal expansion (NTE) [8]. Notably, GeTe exhibits an intrinsic Ge vacancy concentration of 8 to 10% [10], with both the lattice constants and T_c showing composition dependence [11]. These vacancies produce strong p-type conductivity [12] (carrier concentration $\sim 10^{20}$ cm^{-3} [13]), and their coexistence with intrinsic ferroelectric polarization underpins the unique electrical behavior of GeTe.

To date, the thermodynamic and kinetic features of this transformation remain disputed. It was initially classified as a second-order transition due to the shared translational symmetry between the phases and the extrapolation of imaginary phonon frequencies to zero using perturbation theory and self-consistent phonon calculations [14]. Spectroscopic evidence supports this interpretation: inelastic neutron scattering and phonon calculations reveal a triply degenerate phonon condensing at T_c, with similar observations in Raman spectroscopy. Neutron diffraction shows vanishing rhombohedral distortion above T_c, while the concurrent softening of the A_1 and E phonon modes in the Raman spectra of rhombohedral GeTe [8,9] suggests a displacive mechanism. However, subsequent observations of lattice discontinuity [15] and an energy barrier [16] at T_c indicate first-order behavior. Crucially, static extended x-ray absorption fine structure spectroscopy and time-domain terahertz spectroscopy measurements reveal persistent local distortions in cubic GeTe, challenging the purely displacive character and suggesting order-disorder behavior [17–19]. This misinterpretation is often attributed to the averaging effects of diffraction [17]. Similar discussions have emerged in studies of the photoinduced phase transition in GeTe [20–22], and local distortions induced by the PJTE are even known to persist into the liquid phase [23]. We emphasize that this experimental and theoretical discrepancy extends

*Contact author: zmsun@buaa.edu.cn

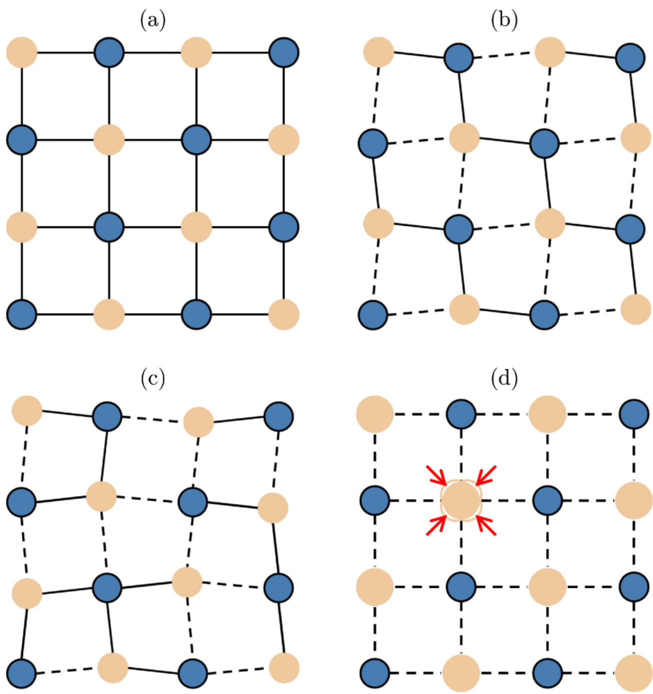

FIG. 1. Schematic illustrations of the atomic structures and ferroelectric transition mechanisms in GeTe. (a) High-temperature cubic phase and (b) low-temperature rhombohedral phase. (c) Order-disorder transition mechanism, featuring random Ge occupations among six $\langle 111\rangle_c$ equilibrium sites above $\boldsymbol{T_c}$. (d) Displacive transition mechanism, characterized by static interatomic displacements induced by vibrational mode condensation. Blue and yellow spheres represent Te and Ge atoms, respectively. Solid and dashed lines denote strong and weak (or dynamic resonant) covalent bonds.

far beyond GeTe, reflecting ongoing debates across other IV-VI compounds [24–30] and hybrid perovskites [31–37].

This brief review highlights that GeTe's seemingly simple structure and composition conceal significant structural complexity. The reversible phase transition can also be driven by pressure and electric fields [38,39], implying a crucial role for electron-lattice coupling [40]. The Jahn-Teller effect and the PJTE are the only recognized sources of spontaneous distortions in high-symmetry polyatomic systems (at $T = 0$ K). In systems with inversion symmetry, spontaneous polar distortions arise exclusively via the PJTE [41]. Consequently, strong vibronic coupling of excited states is the likely driver of the ferroelectric transition. This theoretical framework suggests that local dipole moments may preform in the paraelectric phase through vibronic coupling [42], elegantly explaining phenomena such as the prompt trigonal displacements of Ti ions in $BaTiO_3$ across all ferroelectric and paraelectric phases [43].

In GeTe, the three valence p electrons of any given atom alternate their occupancy among six available bonds, forming an octahedral configuration [12]. Because this bond occupation is degenerate, the half-filled p state introduces a Peierls instability, lowering the energy of its highest occupied states through alternating long/short cation-anion bonds [44]. Within the framework of the PJTE [5], this instability originates from strong vibronic coupling in the excited states: high-symmetry structures (specifically, perfect octahedral configurations) become intrinsically unstable due to degeneracy, inducing symmetry-breaking distortions of the central atom. These distortions force the adiabatic potential energy surface to flatten or form double-well potentials near the equilibrium points under large atomic displacements. Consequently, the harmonic approximation becomes inadequate for describing such vibronic-coupling-induced energy landscapes, directly linking anharmonic lattice vibrations to electronic states.

Despite these foundational insights, a methodological challenge remains: conventional *ab initio* molecular dynamics (AIMD) simulations are often restricted to small supercells (typically hundreds of atoms) and frequently rely on time-averaged spatial analyses. These spatial and temporal constraints can limit the observation of long-range critical fluctuations and obscure instantaneous dynamic orbital hybridizations. Such limitations can complicate interpretations, sometimes producing signatures that resemble discrete order-disorder hopping or obscuring mesoscale domain dynamics. To address these limitations and capture real-time atomic-scale dynamics, we integrated first-principles calculations with large-scale (up to 125 000 atoms) MD simulations driven by NEPs. Moving beyond time-averaged approximations and limited system sizes, we explicitly decouple the spatial and temporal dimensions of the transition. By evaluating the longitudinal current correlation function ($C_L(q,\omega)$) and tracking real-time femtosecond-scale orbital hybridization via tr-COHP, we aim to provide clarifying physical insights into the displacive versus order-disorder debate in GeTe.

II. METHODS

MD provides a robust nonperturbative approach for studying lattice anharmonicity involving significant atomic displacements. Recently developed machine learning potentials overcome the $\mathcal{O}(N^3)$ scaling limitation of AIMD, delivering quantum-mechanically accurate potential energy surfaces at a reduced computational cost [45,46], as demonstrated in recent GeTe studies [3,47–51]. Among these, NEPs achieve higher computational efficiency than Gaussian approximation potentials while maintaining comparable accuracy [52]. Their validity has been well demonstrated in related systems, including PbTe [53], Sb_2Te_3 [54], and GeTe/Sb_2Te_3 superlattices [55]. Here, we employed a NEP model trained on the dataset established by Dangić *et al.* [3,4], integrating it with large-scale MD simulations within the GPUMD package [56], to systematically investigate the microscopic dynamics of the ferroelectric transition in GeTe.

To characterize phonon mode softening, we performed high-precision static single-point energy calculations on the reference dataset [3] using the Vienna *Ab initio* Simulation Package (VASP) [57]. We used the Perdew-Burke-Ernzerhof generalized gradient approximation (GGA-PBE) exchange-correlation functional [58] and projector-augmented wave (PAW) pseudopotentials [59]. Valence electron configurations were set as $4s^2 4p^2$ for Ge and $5s^2 5p^4$ for Te. Electronic convergence was achieved using a 600 eV plane-wave cutoff and a 10^{-7} eV energy threshold, with a k-point sam-

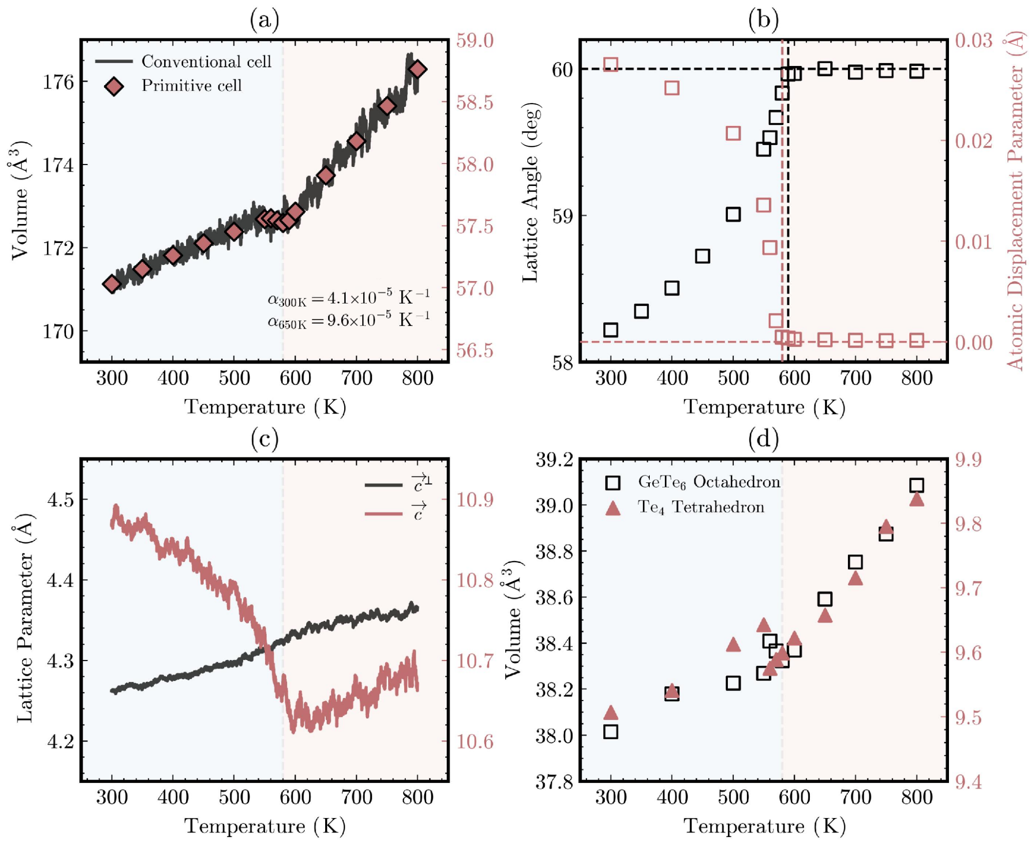

FIG. 2. Macroscopic and microscopic structural evolution across the ferroelectric transition. (a) Volumetric thermal expansion of the conventional (black) and primitive (red) cells, with extracted expansion coefficients annotated. (b) Temperature-dependent rhombohedral angle (black) and Ge atomic displacement parameter (red). Vertical dashed lines indicate the respective critical temperatures. (c) Anisotropic lattice parameter evolution of the conventional rhombohedral cell along and perpendicular to the cubic [111] direction ($\langle 111\rangle_c$). (d) Localized polyhedral volume changes for the distorted $GeTe_6$ octahedra and Te_4 tetrahedra.

pling spacing of 0.1 $Å^{-1}$ (DFT convergence tests: Fig. S1). Structural relaxations were performed to fully optimize the lattice parameters and atomic positions until atomic forces converged below 1 meV/Å.

To isolate the intrinsic structural instability driven by the PJTE without thermal interference, we mapped the adiabatic potential energy surface at 0 K. In an ideal high-symmetry cubic primitive cell ($Fm\bar{3}m$), the central Ge atom was systematically displaced from the octahedral center along the highly symmetric $\langle 100\rangle_c$, $\langle 110\rangle_c$, and $\langle 111\rangle_c$ crystallographic directions. Displacements were applied in fine increments of 0.05 Å, with the cell volume and relative positions of all other atoms strictly constrained to isolate the single-mode potential energy topology. To reflect the inversion symmetry of the reference phase, the resulting energy profiles were fitted to a symmetric double-well polynomial function ($E = \alpha x^2 + \beta x^4$).

Using the NEP-4 framework [60], we developed a GeTe potential with radial and angular cutoff radii of 8 Å. The neural network consists of a single hidden layer containing 70 neurons. The loss function weights were set to 1.0 (energy), 1.0 (atomic forces), and 0.1 (virial stress), with all hyperparameters detailed in Table S1 and Ref. [56]. After 10^6 training iterations, the optimized model achieved root-mean-square errors (RMSEs) of 0.3 meV/atom for energy, 45.7 meV/Å for forces, and 4.2 meV/atom for virial stress (Fig. S2). Thorough validation against DFT-calculated properties—including energy-volume curves, energy surface curves, phonon spectra, and radial distribution functions (Figs. S3–S6)—confirmed the accuracy and transferability of the NEP model.

With a computational efficiency of $\sim 10^6$ atom-steps/second on an NVIDIA GeForce RTX 4090 GPU, this NEP model enables large-scale MD simulations. We constructed ten independent simulation systems using a $17\times17\times7$ supercell of the conventional cell (12 138 atoms) with randomized initial atomic velocities. These systems were heated at a rate of 0.5 K/ps under zero-pressure conditions from 100 K to 800 K. Lattice parameters were derived by averaging trajectory data at each temperature node. As shown in Figs. 2(a)–2(c), this dynamic sampling effectively mitigates thermal fluctuations. It reproduces NTE behavior within the critical phase-transition range, significantly enhancing the accuracy of temperature-dependent lattice parameters compared to traditional methods.

For temperature-dependent effective potential (TDEP) calculations [61,62], we used an $8\times8\times8$ supercell of the primitive cell (1024 atoms). After a 100 ps NVT equilibration to determine temperature-dependent atomic displacement parameters, NVE-ensemble production simulations (1 ns duration, 1 fs timestep) were performed with 2.5 ps sampling intervals. All simulations employed strict initialization protocols, including primitive-cell-derived configurations, unique random velocity seeds, and statistical validation across multiple independent replicas. To capture anharmonic lattice dynamics, we extracted second- to fourth-order interatomic force constants from 400 configurations. The cutoff radii were set to 12 Å (second), 8 Å (third), and 5 Å (fourth), consistent with convergence-tested protocols [51]. Figure S7 displays the calculated temperature-dependent phonon dispersions (white lines) and spectral functions of GeTe.

For rhombohedral GeTe, equilibrium atomic positions were determined by averaging MD snapshots to eliminate the spurious soft longitudinal optical mode at the Γ point. The cubic phase was defined by its ideal positions: Ge at (0.5, 0.5, 0.5) and Te at (0.0, 0.0, 0.0). These positions enabled Crystal Orbital Hamilton Population (COHP) analysis, performed using LOBSTER [63] with matching VASP convergence criteria (600 eV cutoff and 10^{-7} eV threshold).

Furthermore, to capture anharmonic atomic dynamics free from quasiparticle approximations, we calculated the longitudinal current correlation function, $C_L(q, \omega)$, using the DYNASOR package [64]. Derived directly from the velocity-velocity correlation function, $C_L(q, \omega)$ avoids the strong elastic Bragg peak leakage at the Γ point typical of standard dynamic structure factors. Calculations utilized high-frequency unwrapped MD trajectories (10 fs sampling interval) spanning 100 ps. To accurately map the Brillouin zone across the phase transition and prevent finite-size aliasing artifacts, reciprocal space paths were dynamically anchored using the temperature-dependent effective pseudocubic lattice constant (a_{eff}) derived from the volumetric thermal expansion of the supercells.

To address finite-size effects that can obscure phase transition dynamics, we performed supplementary massive-scale NEP-MD simulations containing 125 000 atoms ($N_{\mathrm{Ge}} = N_{\mathrm{Te}} = 62\,500$). We computed the spatial fluctuation correlation function of the local dipoles, $G(\mathbf{r}) = \langle \delta \boldsymbol{P}(0) \cdot \delta \boldsymbol{P}(\mathbf{r}) \rangle$, where δP represents the deviation of the local dipole moment from the macroscopic average. The local dipole of each Ge atom was evaluated based on relative displacements to its nearest Te neighbors within a 3.5 Å cutoff. The spatial correlation length ξ was extracted by fitting the long-range tail ($r > 5$ Å) of $G(r)$ to the three-dimensional Ornstein-Zernike model, $G(r) = A \exp(-r/\xi)/r + B$. Although the baseline B should strictly vanish in the ideal paraelectric phase, it was retained as a free parameter during fitting solely to absorb residual numerical background noise arising from the finite simulation box. The effective finite-size scaling exponent ν_{eff} was subsequently determined by fitting the extracted $\xi(T)$ in the paraelectric phase strictly to the power-law pseudodivergence $\xi(T) = \xi_0(T - T_c)^{-\nu_{\mathrm{eff}}}$.

To capture continuous real-time transition kinetics without finite-size constraints, we performed an unbiased continuous annealing simulation on a 54 000-atom supercell. The system was simulated in a fully flexible isothermal-isobaric ensemble, allowing for unconstrained macroscopic anisotropic distortions. Continuous cooling from 610 K to 560 K was executed over 5 ns (effective cooling rate of 10 K/ns) with a 2.0 fs timestep (Fig. S8). To accurately extract single-atom spatial averages across periodic boundaries, a KDTree spatial partitioning algorithm combined with the minimum image convention was applied during post-processing.

Finally, to track real-time electron-lattice coupling and dynamic orbital hybridization, we performed time-resolved COHP (tr-COHP) analysis. Unlike conventional static COHP evaluations, we extracted 100 consecutive instantaneous snapshots separated by 50 fs from the NEP-MD trajectories at representative temperatures (300 K and 800 K). High-precision static single-point energy calculations were performed on these snapshots using VASP with symmetry explicitly disabled (ISYM $= -1$) to preserve instantaneous dynamic distortions. The resulting delocalized plane-wave wavefunctions were then projected onto local atomic basis sets using the LOBSTER code. To ensure mathematical orthogonality and prevent extreme charge spilling when projecting highly delocalized resonant bonds in the high-temperature phase, unoccupied d orbitals (4d for Ge and 5d for Te) were explicitly introduced as polarization functions alongside an expanded number of empty bands [65].

III. RESULTS AND DISCUSSION

Our MD simulations accurately reproduce both the NTE behavior and lattice anisotropy evolution in GeTe. The heating simulations reveal a ferroelectric phase transition near $T_c \approx 580$ K. The volumetric thermal expansion coefficients of rhombohedral and cubic GeTe are predicted to be 4.1×10^{-5} and 9.6×10^{-5} K^{-1}, respectively, as shown in Fig. 2(a). These results are in reasonable agreement with neutron powder diffraction measurements of 4.59×10^{-5} and 7.67×10^{-5} K^{-1} [8]. The larger coefficient above T_c underscores the critical role of lattice anharmonicity in cubic GeTe at high temperatures. This anharmonic lattice behavior may also be influenced by point defects such as Ge vacancies, which have been proposed to explain the spread in reported transition temperatures [7]. First-principles calculations by Liu *et al.* [66] demonstrated that Ge vacancies stabilize the cubic phase via a lower formation energy and enhanced phonon dynamical stability. Since our training set contained no defective structures, we did not simulate vacancy models. Nevertheless, such defects are expected to further stabilize the cubic phase and thus reduce the transition temperature.

To establish a robust thermodynamic baseline and validate the fidelity of our large-scale NEP model across the phase transition, we first evaluated the macroscopic structural parameters, atomic variances, and the collective order parameter [Figs. 2 and 4(a)–4(c)]. While reproducing these macroscopic averages establishes a necessary baseline, we primarily focus on uncovering the underlying temporal and mesoscale spatial dynamics. Proceeding from this baseline, Fig. 2(b) demonstrates a continuous decay in both the rhombohedral angle and the Ge atomic displacement parameters, exhibiting order-parameter-like behavior without macroscopic discontinuity. The lattice evolution analysis [Fig. 2(c)] reveals pronounced anisotropy in rhombohedral GeTe: expansion perpendicular to the c axis contrasts with parallel contraction. Notably, cubic GeTe retains weak anisotropy above T_c, with linear expansion coefficients $\alpha_c = 3.2\times10^{-5}$ K^{-1} and $\alpha_{c\perp} = 3.0\times10^{-5}$ K^{-1}. Kimber and co-workers attributed this persistent anisotropy to dynamic ferroelectric fluctuations coupled with elasticity [67].

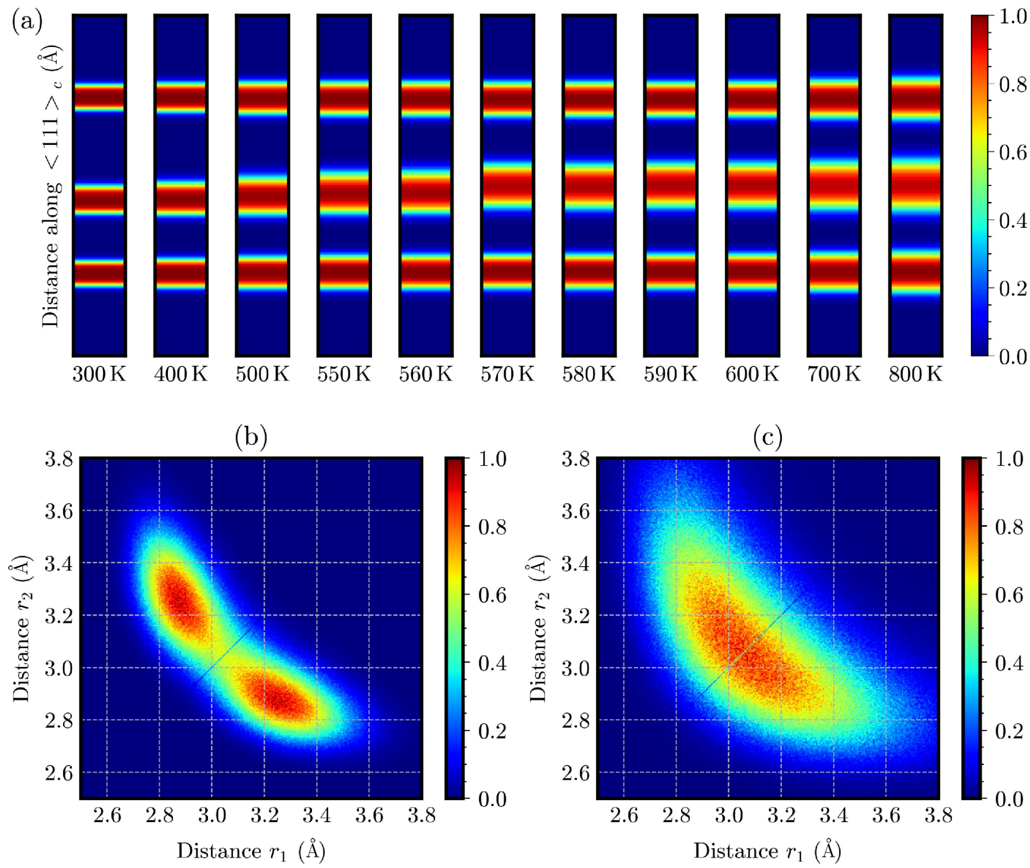

FIG. 3. Atomic distribution and angularly limited three-body correlations during the phase transition in GeTe. (a) Heatmap of the Te-Ge-Te atomic distribution along the $\langle 111 \rangle_c$ crystallographic direction. (b) Rhombohedral GeTe at 300 K. (c) Cubic GeTe at 800 K. Color bars in all panels represent the normalized probability function, with warmer colors denoting higher probabilities.

Earlier first-principles studies attributed the NTE primarily to acoustic/soft transverse optical phonon coupling [68]. Our MD simulations reveal an additional microscopic pathway involving destabilized Te_4 tetrahedra near T_c followed by the cooperative contraction of distorted $GeTe_6$ octahedra [Fig. 2(d)]. The observed contraction may be related to the spatial occupation by lone-pair electrons. Their stereochemical activity induces anisotropic lattice distortion, which modifies elastic properties and drives the NTE, as discussed in systems like $PbTiO_3$ [69]. These findings differ from the vacancy-dominant mechanism reported elsewhere [16], although vacancies likely amplify octahedral contraction. The presence of cation vacancies is expected to cause local atomic displacements toward the vacancy [16], which partially accounts for the volume-change discrepancy between our ideal-lattice simulations ($\Delta V \approx 0.18\%$) and experimental measurements ($\Delta V \approx 0.6\%$) [8].

The minor 10 K critical temperature deviation between the rhombohedral angle (590 K) and the Ge atomic displacement parameter (580 K) further evidences complex transition dynamics, suggesting a two-step phase transition [Fig. 2(b)]. To explicitly verify this two-step mechanism and exclude finite-size artifacts inherent to small simulation boxes, we analyzed the structural evolution from the continuous annealing simulation across the critical region. By monitoring the system on a continuous time axis, we observed a direct temporal decoupling between the macroscopic lattice strain and the microscopic sublattice polarization (Fig. S9). This mesoscale real-space evidence robustly confirms the two-step transition dynamics, corroborating the PJTE as the fundamental microscopic driver.

To explore the atomic dynamics and structural fluctuations of GeTe, we performed MD simulations at varying temperatures using a $17 \times 10 \times 7$ supercell of the orthorhombic cell (14 280 atoms), chosen to streamline data processing. The displacement vector distributions reveal cooperative Ge-layer shifts ($\sim$0.25 Å) along the $\langle 111 \rangle_c$ direction during the transition [Fig. 3(a)]. The probability distributions of the z-components of the Ge atom displacement vectors were fitted to Gaussian functions [Fig. 4(a)]. Despite broadening at elevated temperatures—consistent with increased atomic vibrational amplitudes—all distributions maintain well-defined Gaussian shapes centered at zero displacement. This confirms the absence of dynamic off-centering in our simulations; otherwise, multimodal distributions peaking away from the octahedral center would emerge. This behavior differs from the multistate hopping predicted for order-disorder transitions [Fig. 1(c)], supporting a displacive-driven mechanism in GeTe [Fig. 1(d)].

To elucidate the spatial nature of this structural transformation, we evaluated the role of finite-size effects commonly encountered in MD simulations. Attempts to map the macroscopic free energy surface using enhanced sampling techniques within a conventionally small supercell (e.g.,

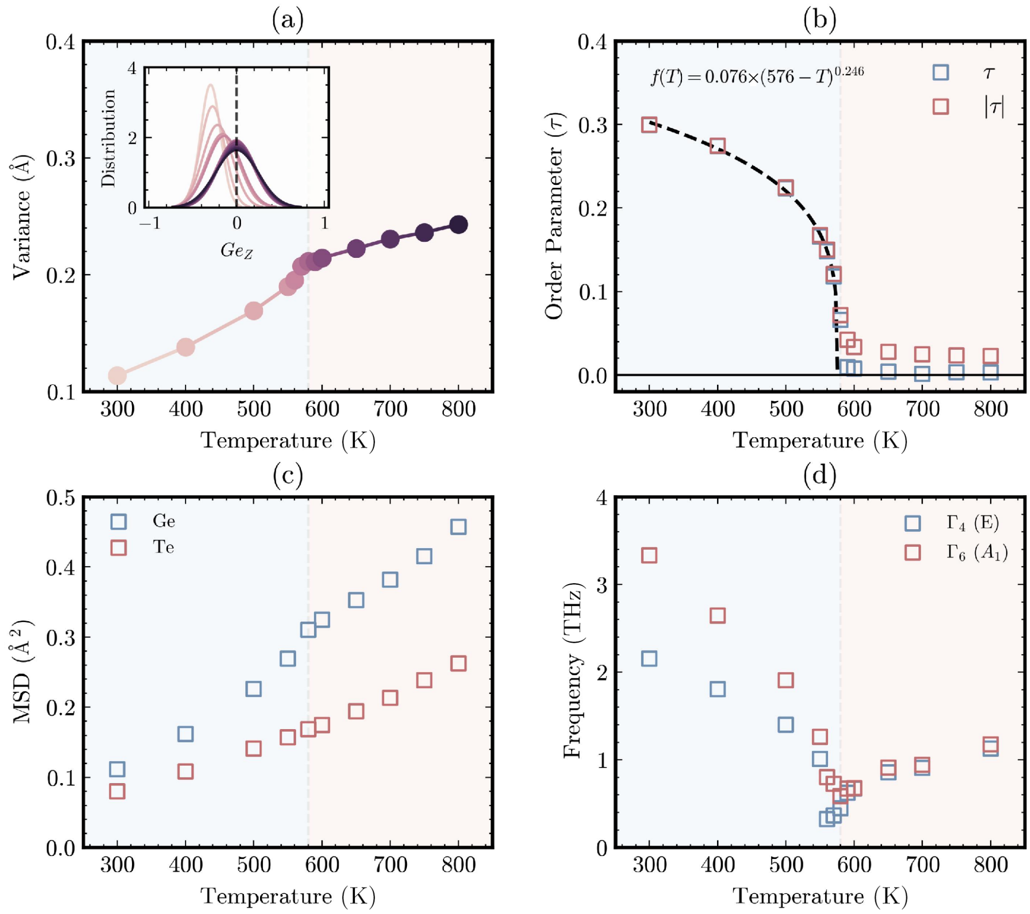

FIG. 4. Thermodynamic and dynamic signatures of the ferroelectric transition. (a) Variance of the Ge displacement vector distribution along the $\langle 111\rangle_c$ direction, with the inset showing the distribution profiles. (b) Temperature dependence of the order parameter $\boldsymbol{\tau}$ (blue) and its mean modulus (red), with the dashed line representing a power-law fit for $T < T_c$. (c) Mean squared displacements (MSDs) of Ge and Te atoms. (d) Frequency evolution of the $\Gamma_4(E)$ and $\Gamma_6(A_1)$ optical phonon modes at the Brillouin zone center.

128 atoms) yielded a massive energy barrier—exceeding several electronvolts per atom—when enforcing a homogeneous, cell-wide polar distortion into a single-domain state. This substantial energetic penalty indicates that imposing uniform macroscopic displacements in small periodic boxes overly constrains lattice shear degrees of freedom, inducing severe steric repulsion. It suggests that the ferroelectric transition in GeTe does not proceed via homogeneous macroscopic displacive shifts. Instead, the transition is governed by local dynamic fluctuations—driven by the PJTE—and the subsequent formation of nanoscale multidomain configurations. This highlights the necessity of mesoscale simulations to accurately capture long-range spatial correlations and domain dynamics without the rigid constraints of small periodic boundaries.

To characterize the displacement behavior of GeTe, we defined the order parameter τ as the displacement of Ge atoms relative to the center of their dynamically moving $GeTe_6$ octahedra. As shown in Fig. 4(b), the order parameter exhibits a critical scaling behavior $\tau(T) \propto (T_c - T)^{\beta}$. Our fitting yields $\beta = 0.246$, approaching the tricritical point universality class prediction (0.25) and aligning with the findings of Yang *et al.* [70].

However, while the macroscopic scaling of the order parameter suggests a pseudocontinuous nature, GeTe is fundamentally a weakly first-order transition system. In our finite-size MD simulations, strong dynamical critical fluctuations near T_c effectively smear out the macroscopic volume and order parameter discontinuities, yielding an apparent continuous scaling near a tricritical point.

Nevertheless, the intrinsic first-order character remains observable at the microscopic level, stemming from two localized structural abruptions at T_c: a two-step transition mechanism revealed by the decoupled deviations in the rhombohedral angle and atomic displacements [Fig. 2(b)], and the stereochemical activity of lone pairs that drives the structural collapse of Te_4 tetrahedra [Fig. 2(d)]. Furthermore, intrinsic vacancy concentrations in experimental samples strongly affect the effective order of the phase transition by suppressing long-range coherence, thereby bridging the apparent gap between pure theoretical models and varied experimental observations.

Our simulations also reveal the preformation of localized dipole moments, consistent with the theoretical framework of the PJTE, which offers a physical explanation for the order-disorder features observed in local structural analyses. Near T_c, we find significant divergence between the order parameter and its average modulus [Fig. 4(b)]. The latter quantities remain constant for $T > T_c$, confirming persistent temperature-independent fluctuations in cubic GeTe. The pair distribution function (PDF) of cubic GeTe exhibits strongly asymmetric peaks without splitting (Fig. S6). Given the absence of static Ge off-centering, this asymmetry likely originates from dynamic octahedral distortions or tilts. Combining mean-square displacement data [Fig. 4(c)] with our MD simulations, we demonstrate that the asymmetry arises from dynamic anharmonic thermal vibrations rather than static atomic displacements. This mechanism is consistent with behavior observed in SnTe and PbTe [28].

We further analyzed the angularly limited three-body correlation function [71–73] to probe the static PJTE. As shown in Figs. 3(b) and 3(c), its periodic correlation progressively decouples with increasing temperature. The function $P(r_1, r_2)$ represents the probability of finding atom C at a distance r_2 from atom B, which lies at a distance r_1 from reference atom A. The angle θ between vectors $\overrightarrow{BA}$ and $\overrightarrow{BC}$ is restricted to 150° to 180°. Residual distortions induced by the PJTE remain observable in cubic GeTe; without such distortions, $P(r_1, r_2)$ would appear as a symmetric circle. These residual distortions align with the observation by Hudspeth *et al.* [74] of ∼20 Å local distortion correlations in cubic GeTe. This microscopic observation is corroborated by our mesoscale simulations, where the extracted spatial correlation length (ξ) reaches macroscopic scales of approximately 25 Å near the critical point (detailed subsequently), indicating that these local distortions are dynamic manifestations of long-range critical fluctuations. Local dipoles persist in the paraelectric phase, consistent with the vibronic ferroelectric theory of the PJTE. The distortions induced by the PJTE are fundamentally dynamic, originating from rapid nuclear fluctuations among equivalent configurations. This ultrafast process, occurring across picosecond to femtosecond timescales, is too rapid to be resolved as static displacements in conventional average structure measurements [42].

Strong anharmonic lattice vibrations in GeTe originate primarily from the PJTE [5]. The quantum mechanical competition between ground and excited states flattens the energy surface at the high-symmetry octahedral configuration ($Q = 0$), promoting the formation of a double-well or multiwell topological landscape. To decouple this intrinsic electronic instability from high-temperature thermal noise, we evaluated the static adiabatic potential energy surface of the cubic phase at 0 K. Displacement of the central Ge atom along the $\langle 100\rangle_c$, $\langle 110\rangle_c$, and $\langle 111\rangle_c$ directions yields characteristic symmetric double-well potentials (Fig. S10), confirming that the ideal octahedral symmetry is intrinsically unstable. Crucially, the energy barriers (ΔE) extracted from symmetric fits between the high-symmetry saddle point and absolute energy minima are 7.6, 10.0, and 11.1 meV/atom for the respective directions. These barrier heights are substantially lower than the thermal fluctuation energy present at the transition temperature ($k_B T_c \approx 51.7$ meV for $T_c \approx 600$ K). The condition $\Delta E \leqslant k_B T_c$ indicates that atoms near T_c execute continuous, high-frequency dynamic sliding upon a shallow potential energy surface, rather than rare, thermally activated jumps across deep static barriers.

The competition between ground and excited p-orbital states drives structural instability and pronounced anharmonicity. While Te atoms exhibit harmonic behavior with linearly temperature-dependent MSDs [Fig. 4(c)], Ge atoms in rhombohedral GeTe display power-law MSD growth, signifying anharmonicity-dominated vibrations. Our TDEP calculations reveal progressive softening of the $\Gamma_4(E)$ and $\Gamma_6(A_1)$ optical phonon frequencies near T_c [Fig. 4(d)], consistent with recent effective harmonic analyses reported by Y. Wang *et al.* [5]. However, while the TDEP approach elegantly captures the macroscopic softening trend, it relies on a time-averaged quasiparticle picture. This approximation may not fully describe the real-time anharmonicity near T_c, complicating the distinction between continuous displacive sliding and discrete order-disorder hopping. To obtain a model-free representation of the phase transition dynamics, we calculated the longitudinal current correlation function $C_L(q, \omega)$ (Fig. S11).

At 300 K, $C_L(q, \omega)$ exhibits well-defined acoustic and optical dispersion branches that match the TDEP results, providing baseline validation. As the temperature approaches T_c, the soft optical mode at the Γ point undergoes overdamped softening, manifesting as a broad spectral weight collapsing toward zero frequency. Notably, the $C_L(q, \omega)$ spectra lack an isolated central quasielastic peak at $\omega = 0$ THz decoupled from the soft phonon branches. If the transition were driven by a thermally activated order-disorder mechanism, a quasielastic scattering signature would typically emerge. Its absence, combined with the continuous overdamped softening of the optical mode and the asymmetrically synchronized power-law growth in atomic displacement variances [Fig. 4(a)], further supports the conclusion that the structural transformation in GeTe is a displacive phase transition driven by anharmonic fluctuations.

To evaluate the length scale of these dynamic fluctuations and address finite-size effects commonly encountered in previous AIMD studies, we analyzed the massive-scale NEP-MD simulations containing 125 000 atoms ($N_{\mathrm{Ge}} = N_{\mathrm{Te}} = 62,500$). By evaluating the spatial fluctuation correlation function of local dipoles, $G(r)$ (Fig. S12), we observed a pronounced "long tail" emerging near T_c, visualizing the long-range critical fluctuations characteristic of a displacive transition. The extracted spatial correlation length ξ peaks at approximately 25 Å near the critical point (Fig. S13). This mesoscopic length scale highlights a limitation in earlier AIMD studies: simulation boxes containing only 512 atoms may physically truncate these critical fluctuations. By artificially bounding ξ, small-scale simulations inadvertently enforce rigid structural constraints, potentially producing artifacts resembling discrete multistate hopping. Our large-scale NEP simulation safely encompasses this correlation length, providing thermodynamic support for a transition governed by correlated anharmonic fluctuations.

Furthermore, fitting the paraelectric regime to the pseudocritical scaling law $\xi(T) \propto (T - T_c)^{-\nu_{\mathrm{eff}}}$ yields a Curie-Weiss fluctuation temperature $T_c = 560.9$ K and an effective finite-size scaling exponent $\nu_{\mathrm{eff}} = 0.32$. Notably, this value is exceptionally close to $\nu_{\mathrm{eff}} = 1/d \approx 0.33$ (where $d = 3$ is the spatial dimensionality), which is the well-established theoretical signature characterizing the pseudodivergence of a first-order phase transition under finite-size scaling [75,76]. This mesoscopic scaling result mathematically corroborates

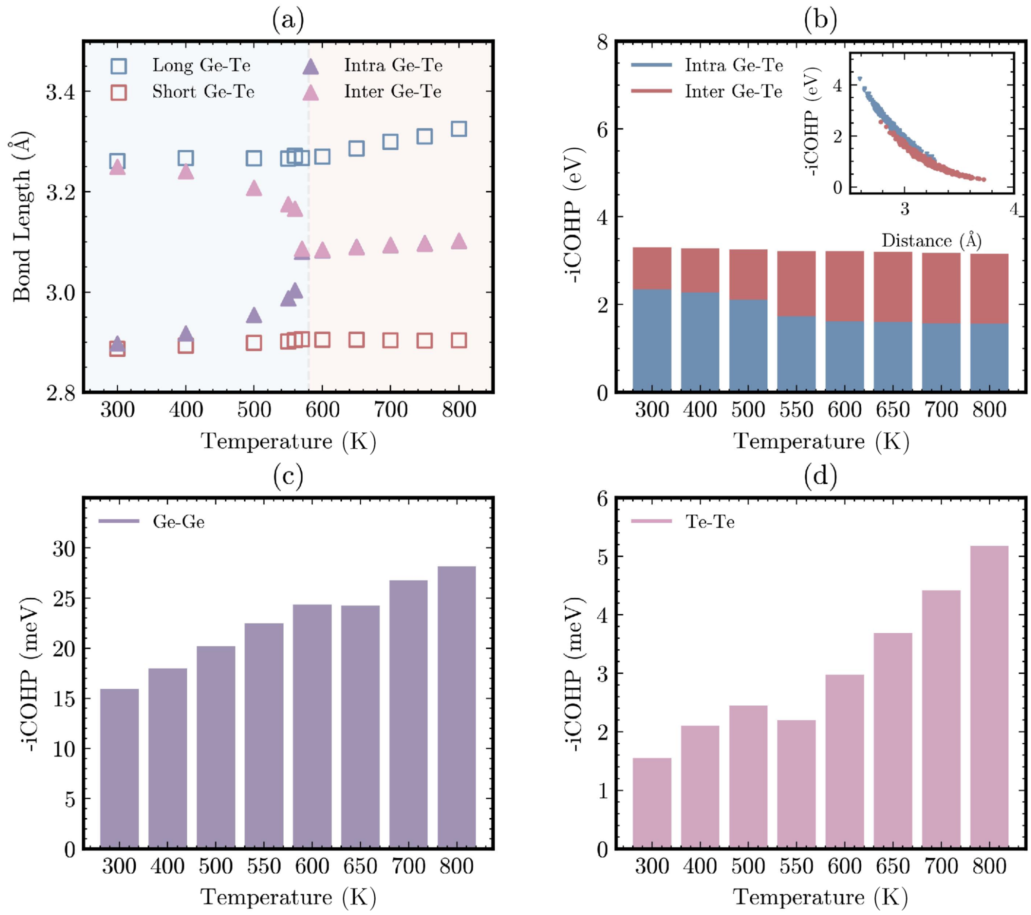

FIG. 5. Chemical bonding evolution across the phase transition. (a) Temperature dependence of Ge-Te bond lengths. Boxes denote the averages of the three longest/shortest bonds within each $GeTe_6$ octahedron; triangles represent averaged intra- and interlayer bonds. (b) Absolute values of the integrated Crystal Orbital Hamilton Population (-iCOHP) for intra- (blue) and interlayer (red) Ge-Te bonds. Inset: -iCOHP versus bond length. (c), (d) Evolution of the -iCOHP for next-nearest-neighbor Ge-Ge (c) and Te-Te (d) bonds.

our earlier deduction that GeTe undergoes a weakly first-order transition, while still being governed by strongly correlated anharmonic fluctuations. Detailed methodologies for the correlation function and critical scaling evaluations are provided in Supplemental Note 1 [77].

Like many chalcogenides, GeTe exhibits strong chemical bond-length constraints [78–80], with both short and long Ge-Te bonds displaying covalent character [79]. GeTe possesses anomalously large Born effective charges [81] arising from dynamic charge transfer during atomic displacements. Valence electrons rapidly reorganize via orbital hybridization, mitigating energy increases from lattice distortion and enabling spontaneous symmetry breaking in flexible $GeTe_6$ octahedra. The synergy between covalent bonding, coherent lattice dynamics, and responsive electronic behavior underpins the functional properties of GeTe. We systematically quantified nearest and next-nearest-neighbor bond-length evolution and bond-order stability across 300 to 800 K.

While global scalar averages of short and long bonds provide useful statistics, they can obscure directional collective dynamics. Therefore, we explicitly defined the intralayer (in-plane) and interlayer (out-of-plane) bonds along the $\langle 111 \rangle_c$ polarization direction [Fig. 3(a)] to capture the cooperative collective shift of Ge layers. As shown in Fig. 5(a), while the globally averaged short and long Ge-Te bonds exhibit negligible temperature dependence, the directionally resolved intralayer and interlayer bonds converge perfectly at T_c.

Remarkably, the absolute value of the averaged integrated Crystal Orbital Hamilton Population (-iCOHP) for Ge-Te bonds remains thermally stable [Fig. 5(b)], despite a redistribution of intra- and interlayer bonding interactions between 300 K and 800 K. This confirms octahedral reconfiguration via resonant bonding networks on an ultrafast timescale. Within this dynamic picture, Ge atoms maintain the distorted bond-length distribution characteristic of the PJTE through continuous bond-order adjustments, effectively avoiding the central potential barrier.

While static or time-averaged radial distribution functions (RDF) and bond analyses capture local geometrical asymmetry, they blur the temporal axis, making it difficult to distinguish between rare, thermally activated discrete jumps and continuous, high-frequency sliding. To decouple the spatial and temporal dimensions and extract detailed dynamical information, we employed tr-COHP analysis to monitor real-time dynamic resonant bonding.

Isolating the three pairs of opposite Ge-Te bonds along the pseudocubic axes within a single $GeTe_6$ octahedron reveals a contrast in dynamic bonding between the low- and high-temperature phases. At 300 K, the structural distortion induced by the PJTE is largely frozen. The pairwise bonds exhibit a rigid hierarchy: three strong covalent bonds maintain high -iCOHP values (2.0 to 3.5 eV), while the three opposite weak bonds are suppressed (below 1.5 eV), with no crossover events observed across the temporal trajectory [Fig. S14(a)].

At 800 K, despite the macroscopic restoration of the ideal $Fm\bar{3}m$ cubic symmetry according to average atomic positions, microscopic orbital interactions behave differently. The static hierarchy collapses, and the -iCOHP values of individual Ge-Te bonds exhibit high-frequency oscillations spanning 0.1 eV to nearly 5.0 eV [Fig. S14(b)]. The opposite pairs of Ge-Te bonds exhibit a pronounced "seesaw" effect characterized by a strong negative correlation (Pearson r reaching up to -0.81). When one Ge-Te bond strengthens into a covalent state, its opposing counterpart weakens into an antibonding-like state.

This phenomenon—where the negative correlation intensifies at higher temperatures—differs from expectations for a classical order-disorder model, where high thermal noise would randomize atomic hopping and degrade pairwise bonding correlations. The presence of synchronized parity flipping at 800 K indicates that the local disorder involves coherent, ultrafast charge transfer (dynamic orbital hybridization) coupled with soft transverse optical phonons. The persistent local distortions in cubic GeTe can thus be viewed as femtosecond-scale snapshots of continuous anharmonic vibrations on a flat PJTE potential energy surface, supporting a dynamically displacive transition.

Analysis of next-nearest-neighbor bonds reveals an anomalous trend: despite their weak covalent character, -iCOHP values for Ge-Ge and Te-Te bonds generally increase with temperature [Figs. 5(c) and 5(d)]. This behavior contrasts with conventional thermal expansion expectations. Kielar *et al.* previously attributed enhanced thermal conductivity near T_c to next-nearest-neighbor bond strengthening [82]. However, this interpretation warrants further examination, as second-neighbor bonds strengthen even in rhombohedral GeTe. The minimal structural evolution at the Te sublattice restricts the local distortion amplitudes of the PJTE. Progressive bond stiffening would further rigidify the lattice, driving more isotropic Ge distributions within $GeTe_6$ octahedra [Fig. 1(d)]. This constraint produces effects analogous to compressive hydrostatic stress [33], where bond-strength redistribution similarly restrains atomic displacements.

IV. CONCLUSIONS

In summary, this study provides a comprehensive dynamical model for the ferroelectric phase transition in GeTe by integrating first-principles calculations with large-scale NEP-MD simulations. We identify a displacive transformation near a tricritical point and highlight the role of the pseudo-Jahn-Teller effect (PJTE), revealing the coexistence of local dynamic distortions and macroscopic long-range order. At low temperatures, cooperative dipole alignment establishes ferroelectric ordering, whereas thermal anharmonicity at elevated temperatures disrupts this cooperativity, driving collective Ge displacements toward the octahedral centers. Crucially, our tr-COHP analysis provides compelling evidence against the classical order-disorder hopping mechanism. We show that the apparent local disorder in the cubic phase originates from a continuous, high-frequency "seesaw" charge transfer—a dynamic resonant bonding process driven by the PJTE on a remarkably flat adiabatic potential energy surface. This "macro-ordered yet micro-disordered" paradigm offers a nuanced perspective on conventional phase-transition classifications, helping to clarify long-standing controversies surrounding GeTe. Ultimately, our findings provide fundamental insights into anharmonic dynamics and correlated structural distortions in IV-VI compounds, which can inform the rational design of their thermal and optoelectronic properties.

ACKNOWLEDGMENT

This work was supported by the National Natural Science Foundation of China (Grant No. 52332005).

DATA AVAILABILITY

The data that support the findings of this study are available from the corresponding author upon reasonable request.

[1] J. E. Boschker, R. Wang, and R. Calarco, GeTe: A simple compound blessed with a plethora of properties, CrystEngComm **19**, 5324 (2017).
[2] K. Singh, S. Kumari, H. Singh, N. Bala, P. Singh, A. Kumar, and A. Thakur, A review on GeTe thin film-based phase-change materials, Appl. Nanosci. **13**, 95 (2023).
[3] Đ. Dangić, O. Hellman, S. Fahy, and I. Savić, The origin of the lattice thermal conductivity enhancement at the ferroelectric phase transition in GeTe, npj Comput. Mater. **7**, 57 (2021).
[4] Đ. Dangić, S. Fahy, and I. Savić, Molecular dynamics simulation of the ferroelectric phase transition in GeTe: Displacive or order-disorder character, Phys. Rev. B **106**, 134113 (2022).
[5] Y. Wang, M. Hu, L. Xie, and J. He, Orbit-lattice coupling leads to the intrinsic low thermal conductivity in M Te (M = Ge, Sn, Pb) thermoelectric materials, Phys. Rev. B **109**, 205204 (2024).
[6] T. Chattopadhyay, J. X. Boucherle, and H. G. vonSchnering, Neutron diffraction study on the structural phase transition in GeTe, J. Phys. C: Solid State Phys. **20**, 1431 (1987).
[7] U. D. Wdowik, K. Parlinski, S. Rols, and T. Chatterji, Soft-phonon mediated structural phase transition in GeTe, Phys. Rev. B **89**, 224306 (2014).
[8] T. Chatterji, C. M. N. Kumar, and U. D. Wdowik, Anomalous temperature-induced volume contraction in GeTe, Phys. Rev. B **91**, 054110 (2015).
[9] M. J. Polking *et al.*, Size-dependent polar ordering in colloidal GeTe nanocrystals, Nano Lett. **11**, 1147 (2011).
[10] A. V. Kolobov, J. Tominaga, P. Fons, and T. Uruga, Local structure of crystallized GeTe films, Appl. Phys. Lett. **82**, 382 (2003).
[11] E. M. Levin, M. F. Besser, and R. Hanus, Electronic and thermal transport in GeTe: A versatile base for thermoelectric materials, J. Appl. Phys. **114**, 083713 (2013).

[12] A. Edwards, A. Pineda, P. Schultz, M. Martin, A. Thompson, H. Hjalmarson, and C. Umrigar, Electronic structure of intrinsic defects in crystalline germanium telluride, Phys. Rev. B **73**, 045210 (2006).

[13] T. Siegrist, P. Jost, H. Volker, M. Woda, P. Merkelbach, C. Schlockermann, and M. Wuttig, Disorder-induced localization in crystalline phase-change materials, Nat. Mater. **10**, 202 (2011).

[14] Y. Xia and M. K. Y. Chan, Anharmonic stabilization and lattice heat transport in rocksalt β-GeTe, Appl. Phys. Lett. **113**, 193902 (2018).

[15] J. M. Leger and A. M. Redon, Phase transformations and volume of the IV-VI GeTe semiconductor under high pressure, J. Phys.: Condens. Matter **2**, 5655 (1990).

[16] M. Sist, H. Kasai, E. M. J. Hedegaard, and B. B. Iversen, Role of vacancies in the high-temperature pseudodisplacive phase transition in GeTe, Phys. Rev. B **97**, 094116 (2018).

[17] P. Fons, A. V. Kolobov, M. Krbal, J. Tominaga, K. S. Andrikopoulos, S. N. Yannopoulos, G. A. Voyiatzis, and T. Uruga, Phase transition in crystalline GeTe: Pitfalls of averaging effects, Phys. Rev. B **82**, 155209 (2010).

[18] T. Matsunaga, P. Fons, A. V. Kolobov, J. Tominaga, and N. Yamada, The order-disorder transition in GeTe: Views from different length-scales, Appl. Phys. Lett. **99**, 231907 (2011).

[19] M. Xu, Z. Lei, J. Yuan, K. Xue, Y. Guo, S. Wang, X. Miao, and R. Mazzarello, Structural disorder in the high-temperature cubic phase of GeTe, RSC Adv. **8**, 17435 (2018).

[20] N.-K. Chen, X.-B. Li, J. Bang, X.-P. Wang, D. Han, D. West, S. Zhang, and H.-B. Sun, Directional forces by momentumless excitation and order-to-order transition in Peierls-distorted solids: The case of GeTe, Phys. Rev. Lett. **120**, 185701 (2018).

[21] L. Chen, L. Wang, K. Jiang, J. Zhang, Y. Li, L. Shang, L. Zhu, S. Gong, and Z. Hu, Optically induced multistage phase transition in coherent phonon-dominated a-GeTe, J. Phys. Chem. Lett. **14**, 5760 (2023).

[22] M. Furci, G. Marini, and M. Calandra, First-order rhombohedral-to-cubic phase transition in photoexcited GeTe, Phys. Rev. Lett. **132**, 236101 (2024).

[23] J. Y. Raty, V. Godlevsky, Ph. Ghosez, C. Bichara, J. P. Gaspard, and J. R. Chelikowsky, Evidence of a reentrant Peierls distortion in liquid GeTe, Phys. Rev. Lett. **85**, 1950 (2000).

[24] E. S. Božin, C. D. Malliakas, P. Souvatzis, T. Proffen, N. A. Spaldin, M. G. Kanatzidis, and S. J. L. Billinge, Entropically stabilized local dipole formation in lead chalcogenides, Science **330**, 1660 (2010).

[25] S. Kastbjerg, N. Bindzus, M. Søndergaard, S. Johnsen, N. Lock, M. Christensen, M. Takata, M. A. Spackman, and B. Brummerstedt Iversen, Direct evidence of cation disorder in thermoelectric lead chalcogenides PbTe and PbS, Adv. Funct. Mater. **23**, 5477 (2013).

[26] T. Keiber, F. Bridges, and B. C. Sales, Lead is not off center in PbTe: The importance of *r*-space phase information in extended x-ray absorption fine structure spectroscopy, Phys. Rev. Lett. **111**, 095504 (2013).

[27] K. R. Knox, E. S. Bozin, C. D. Malliakas, M. G. Kanatzidis, and S. J. L. Billinge, Local off-centering symmetry breaking in the high-temperature regime of SnTe, Phys. Rev. B **89**, 014102 (2014).

[28] C. W. Li *et al.*, Anharmonicity and atomic distribution of SnTe and PbTe thermoelectrics, Phys. Rev. B **90**, 214303 (2014).

[29] K. V. Mitrofanov, A. V. Kolobov, P. Fons, M. Krbal, T. Shintani, J. Tominaga, and T. Uruga, Local structure of the SnTe topological crystalline insulator: Rhombohedral distortions emerging from the rocksalt phase, Phys. Rev. B **90**, 134101 (2014).

[30] M. Sist, E. M. Jensen Hedegaard, S. Christensen, N. Bindzus, K. F. F. Fischer, H. Kasai, K. Sugimoto, and B. Brummerstedt Iversen, Carrier concentration dependence of structural disorder in thermoelectric $Sn_{1-x}Te$, IUCrJ **3**, 377 (2016).

[31] M. Paściak, T. R. Welberry, J. Kulda, S. Leoni, and J. Hlinka, Dynamic displacement disorder of cubic $BaTiO_3$, Phys. Rev. Lett. **120**, 167601 (2018).

[32] S. Salmani-Rezaie, K. Ahadi, W. M. Strickland, and S. Stemmer, Order-disorder ferroelectric transition of strained $SrTiO_3$, Phys. Rev. Lett. **125**, 087601 (2020).

[33] M. Kotiuga, S. Halilov, B. Kozinsky, M. Fornari, N. Marzari, and G. Pizzi, Microscopic picture of paraelectric perovskites from structural prototypes, Phys. Rev. Res. **4**, L012042 (2022).

[34] X.-G. Zhao, O. I. Malyi, S. J. L. Billinge, and A. Zunger, Intrinsic local symmetry breaking in nominally cubic paraelectric $BaTiO_3$, Phys. Rev. B **105**, 224108 (2022).

[35] J. Očenášek, J. Minár, and J. Alcalá, Dynamics of lattice disorder in perovskite materials, polarization nanoclusters and ferroelectric domain wall structures, npj Comput. Mater. **9**, 118 (2023).

[36] K. Kurushima, H. Nakajima, T. Ogata, Y. Sakai, M. Azuma, and S. Mori, Relationship between Pb ion off-centering and lone pair electrons, Sci. Rep. **15**, 9314 (2025).

[37] C. Mao *et al.*, Correlated dynamic disorder, octahedral tilts, and acoustic phonon softening in $CsSnBr_3$ and $CsPbBr_3$, Phys. Rev. Mater. **9**, 065401 (2025).

[38] Z. Sun, J. Zhou, H.-K. Mao, and R. Ahuja, Peierls distortion mediated reversible phase transition in GeTe under pressure, Proc. Natl Acad. Sci. USA **109**, 5948 (2012).

[39] K. Jeong, H. Lee, C. Lee, L. H. Wook, H. Kim, E. Lee, and M.-H. Cho, Ferroelectric switching in GeTe through rotation of lone-pair electrons by Electric field-driven phase transition, Appl. Mater. Today **24**, 101122 (2021).

[40] D. Campi, D. Donadio, G. C. Sosso, J. Behler, and M. Bernasconi, Electron-phonon interaction and thermal boundary resistance at the crystal-amorphous interface of the phase change compound GeTe, J. Appl. Phys. **117**, 015304 (2015).

[41] I. B. Bersuker, Pseudo-Jahn–Teller effect—A two-state paradigm in formation, deformation, and transformation of molecular systems and solids, Chem. Rev. **113**, 1351 (2013).

[42] I. B. Bersuker, Jahn–Teller and Pseudo-Jahn–Teller effects: From particular features to general tools in exploring molecular and solid state properties, Chem. Rev. **121**, 1463 (2021).

[43] I. B. Bersuker and V. Polinger, Perovskite crystals: Unique pseudo-Jahn–Teller origin of ferroelectricity, multiferroicity, permittivity, flexoelectricity, and polar nanoregions, Condens. Matter **5**, 68 (2020).

[44] J.-P. Gaspard, A. Pellegatti, F. Marinelli, and C. Bichara, Peierls instabilities in covalent structures I. Electronic structure, cohesion and the $Z = 8-N$ rule, Philos. Mag. B **77**, 727 (1998).

[45] P. Friederich, F. Häse, J. Proppe, and A. Aspuru-Guzik, Machine-learned potentials for next-generation matter simulations, Nat. Mater. **20**, 750 (2021).

[46] E. Kocer, T. W. Ko, and J. Behler, Neural network potentials: A concise overview of methods, Annu. Rev. Phys. Chem. **73**, 163 (2022).

[47] G. C. Sosso, G. Miceli, S. Caravati, J. Behler, and M. Bernasconi, Neural network interatomic potential for the phase change material GeTe, Phys. Rev. B **85**, 174103 (2012).
[48] Y.-J. Choi and S.-H. Jhi, Efficient training of machine learning potentials by a randomized atomic-system generator, J. Phys. Chem. B **124**, 8704 (2020).
[49] C. Wang, J. Wu, Z. Zeng, J. Embs, Y. Pei, J. Ma, and Y. Chen, Soft-mode dynamics in the ferroelectric phase transition of GeTe, npj Comput. Mater. **7**, 118 (2021).
[50] J. Zhang, F. Zhang, D. Wei, L. Liu, X. Liu, D. Fang, G. X. Zhang, X. Chen, and D. Wang, Structural phase transition of monochalcogenides investigated with machine learning, Phys. Rev. B **105**, 094116 (2022).
[51] S.-H. Lee, J. Li, V. Olevano, and B. Sklénard, Equivariant graph neural network interatomic potential for Green-Kubo thermal conductivity in phase change materials, Phys. Rev. Mater. **8**, 033802 (2024).
[52] Z. Fan, Z. Zeng, C. Zhang, Y. Wang, K. Song, H. Dong, Y. Chen, and T. Ala-Nissila, Neuroevolution machine learning potentials: Combining high accuracy and low cost in atomistic simulations and application to heat transport, Phys. Rev. B **104**, 104309 (2021).
[53] R. Cheng, X. Shen, S. Klotz, Z. Zeng, Z. Li, A. Ivanov, Y. Xiao, L.-D. Zhao, F. Weber, and Y. Chen, Lattice dynamics and thermal transport of PbTe under high pressure, Phys. Rev. B **108**, 104306 (2023).
[54] K. Li, B. Liu, J. Zhou, and Z. Sun, Revealing the crystallization dynamics of Sb–Te phase change materials by large-scale simulations, J. Mater. Chem. C **12**, 3897 (2024).
[55] B. Wang, K. Li, W. Zhang, Y. Sun, J. Zhou, and Z. Sun, Thermal transport of GeTe/Sb_2Te_3 superlattice by large-scale molecular dynamics with machine-learned potential, J. Phys. Chem. C **129**, 6386 (2025).
[56] Z. Fan *et al.*, GPUMD: A package for constructing accurate machine-learned potentials and performing highly efficient atomistic simulations, J. Chem. Phys. **157**, 114801 (2022).
[57] G. Kresse and J. Hafner, *Ab initio* molecular dynamics for liquid metals, Phys. Rev. B **47**, 558 (1993).
[58] J. P. Perdew, K. Burke, and M. Ernzerhof, Generalized gradient approximation made simple, Phys. Rev. Lett. **77**, 3865 (1996).
[59] P. E. Blöchl, Projector augmented-wave method, Phys. Rev. B **50**, 17953 (1994).
[60] K. Song *et al.*, General-purpose machine-learned potential for 16 elemental metals and their alloys, Nat. Commun. **15**, 10208 (2024).
[61] O. Hellman and I. A. Abrikosov, Temperature-dependent effective third-order interatomic force constants from first principles, Phys. Rev. B **88**, 144301 (2013).
[62] F. Bottin, J. Bieder, and J. Bouchet, a-TDEP: Temperature dependent effective potential for abinit–Lattice dynamic properties including anharmonicity, Comput. Phys. Commun. **254**, 107301 (2020).
[63] S. Maintz, V. L. Deringer, A. L. Tchougréeff, and R. Dronskowski, LOBSTER: A tool to extract chemical bonding from plane-wave based DFT, J. Comput. Chem. **37**, 1030 (2016).
[64] E. Fransson, M. Slabanja, P. Erhart, and G. Wahnström, DYNASOR—A tool for extracting dynamical structure factors and current correlation functions from molecular dynamics simulations, Adv. Theory Simul. **4**, 2000240 (2021).
[65] V. L. Deringer, A. L. Tchougréeff, and R. Dronskowski, Crystal orbital Hamilton population (COHP) analysis as projected from plane-wave basis sets, J. Phys. Chem. A **115**, 5461 (2011).
[66] Z. Liu, N. Sato, Q. Guo, W. Gao, and T. Mori, Shaping the role of germanium vacancies in germanium telluride: Metastable cubic structure stabilization, band structure modification, and stable N-type conduction, NPG Asia Mater. **12**, 66 (2020).
[67] S. A. J. Kimber *et al.*, Dynamic crystallography reveals spontaneous anisotropy in cubic GeTe, Nat. Mater. **22**, 311 (2023).
[68] Đ. Dangić, A. R. Murphy, É. D. Murray, S. Fahy, and I. Savić, Coupling between acoustic and soft transverse optical phonons leads to negative thermal expansion of GeTe near the ferroelectric phase transition, Phys. Rev. B **97**, 224106 (2018).
[69] E. T. Ritz and N. A. Benedek, Interplay between phonons and anisotropic elasticity drives negative thermal expansion in $PbTiO_3$, Phys. Rev. Lett. **121**, 255901 (2018).
[70] D. Yang, T. Chatterji, J. A. Schiemer, and M. A. Carpenter, Strain coupling, microstructure dynamics, and acoustic mode softening in germanium telluride, Phys. Rev. B **93**, 144109 (2016).
[71] C. Bichara, A. Pellegatti, and J.-P. Gaspard, Properties of liquid group-V elements: A numerical tight-binding simulation, Phys. Rev. B **47**, 5002 (1993).
[72] G. Zhao, C. S. Liu, and Z. G. Zhu, *Ab initio* molecular dynamics simulations on structure change of liquid Te from normal-to supercooled-state, J. Phys.: Condens. Matter **20**, 335102 (2008).
[73] C. Wang, Altbc-Analyzer, https://github.com/wangchr1617/altbc_analyzer.
[74] J. M. Hudspeth, T. Chatterji, S. J. L. Billinge, and S. A. J. Kimber, Unifying local and average structure in the phase change material GeTe, arXiv:1506.08944.
[75] M. E. Fisher and A. N. Berker, Scaling for first-order phase transitions in thermodynamic and finite systems, Phys. Rev. B **26**, 2507 (1982).
[76] K. Binder, Theory of first-order phase transitions, Rep. Prog. Phys. **50**, 783 (1987).
[77] See Supplemental Material at http://link.aps.org/supplemental/10.1103/w7ll-dsct for details on NEP model training parameters, DFT convergence tests, additional structural and dynamic analyses, and critical scaling analysis.
[78] M. Wuttig, V. L. Deringer, X. Gonze, C. Bichara, and J. Raty, Incipient metals: Functional materials with a unique bonding mechanism, Adv. Mater. **30**, 1803777 (2018).
[79] J.-Y. Raty and M. Wuttig, The interplay between Peierls distortions and metavalent bonding in IV–VI compounds: Comparing GeTe with related monochalcogenides, J. Phys. Appl. Phys. **53**, 234002 (2020).
[80] R. O. Jones, S. R. Elliott, and R. Dronskowski, The myth of "metavalency" in phase-change materials, Adv. Mater. **35**, 2300836 (2023).
[81] U. V. Waghmare, N. A. Spaldin, H. C. Kandpal, and R. Seshadri, First-principles indicators of metallicity and cation off-centricity in the IV-VI rocksalt chalcogenides of divalent Ge, Sn, and Pb, Phys. Rev. B **67**, 125111 (2003).
[82] S. Kielar, C. Li, H. Huang, R. Hu, C. Slebodnick, A. Alatas, and Z. Tian, Anomalous lattice thermal conductivity increase with temperature in cubic GeTe correlated with strengthening of second-nearest neighbor bonds, Nat. Commun. **15**, 6981 (2024).